Multiple-scattering calculations of x-ray-absorption spectra

S. I. Zabinsky, J. J. Rehr, and A. Ankudinov
Department of Physics, University of Washington, Seattle, Washington 98195

R. C. Albers
Theoretical Division, Los Alamos National Laboratory, Los Alamos, New Mexico 87545

M. J. Eller
Microsoft Corporation, Redmond, Washington 98052
(Received 31 October 1994)

A high-order multiple-scattering (MS) approach to the calculation of polarized x-ray-absorption spectra, which includes both x-ray-absorption fine structure and x-ray-absorption near-edge structure, is presented. Efficient calculations in arbitrary systems are carried out by using a curved-wave MS path formalism that ignores negligible paths, and has an energy-dependent self-energy and MS Debye-Waller factors. Embedded-atom background absorption calculations on an absolute energy scale are included. The theory is illustrated for metallic Cu, Cd, and Pt. For these cases the MS expansion is found to converge to within typical experimental accuracy, both to experiment and to full MS theories (e.g., band structure), by using only a few dozen important paths, which are primarily single-scattering, focusing, linear, and triangular.

I. INTRODUCTION

The interpretation of x-ray-absorption fine structure (XAFS) as a sum over multiple-scattering (MS) paths has been the basis of the theory[1] for many years, and is especially useful in the interpretation of experiments.[2] The absorption fine structure χ is defined as the normalized oscillatory part of the x-ray-absorption cross section $\mu(E)$, i.e., $\chi = (\mu - \mu_0)/\Delta\mu_0$, where μ_0 is the embedded-atom background absorption,[3,4] and $\Delta\mu_0$ is the jump in the background at the edge. The dominant single-scattering (SS) term, due to the path from the absorbing atom to the nearest neighbor and back, is commonly used as a tool to determine accurate near-neighbor distances in solids and molecules. Although it has long been recognized that MS terms are generally needed to describe the structure beyond the nearest-neighbor distance,[1] there has been considerable controversy about the nature and the extent of MS in XAFS.[5] To address this question, we have devised a strategy for high-order MS calculations that greatly speeds up the path-by-path approach. Our method explicitly incorporates loss terms and MS Debye-Waller (DW) factors, which aid convergence and are essential for the success of a short-range-order XAFS theory. For us, the introduction of an efficient path-enumeration algorithm is crucial, since our aim is to obtain convergence of the MS expansion to full multiple-scattering accuracy in extended systems, without the need for symmetry or matrix diagonalizations. In a preliminary presentation of our method, we found that XAFS can be calculated to within experimental accuracy by using about 100 paths.[5] In contrast, full MS diagonalization methods such as band-structure techniques, which calculate x-ray spectra without loss, must introduce broadening effects phenomenologically. Such methods are inefficient, since they calculate excessively detailed fine structure and then broaden much of it away.

Our treatment was originally intended for the moderate-energy to high-energy region above threshold, i.e., the extended-XAFS (EXAFS) regime of about 30–1500 eV above the absorption edge, where the mean free path is relatively short (< 20 Å). However, using the "extended-continuum" model,[6,7] we have augmented our treatment to include the near-edge regime, i.e., the near-edge XAFS and x-ray-absorption near-edge structure (XANES).[8] The application of a high-order path-by-path MS approach in XANES is not, *a priori*, well justified for a number of reasons. These include strong-scattering events at low energies that may destroy convergence of the MS expansion, and chemical and many-electron effects that can alter the scattering amplitudes. Indeed, it has been thought that full MS calculations[1,7,9,10] are needed to describe XANES, especially the many interesting near-edge features such as shape resonances and whitelines, while drastically limited calculations[11,12] suffice at higher energies. Thus, our study also aims to probe the limitations of the MS approach.

In this paper, we present a more thorough and complete exposition of our method than was done previously. In addition, we describe a generalization of our approach for calculations of the polarized x-ray-absorption spectrum $\mu(E)$ on an absolute energy scale, including the continuum near-edge region. Except for our preliminary treatment[5,8] and for small molecules, finite MS calculations have generally been limited to small molecules and clusters, or to third order scattering processes.[7,12,13] The most definitive calculations of XAFS in extended systems have been based on full MS band-structure methods.[14–17]

These methods are limited to crystalline geometries and low photoelectron energies ($E \leq 150$ eV). They often neglect the core hole, since they assume full periodicity. (The absorbing atom is treated as identical to similar atoms in other unit cells.) They have also not included an energy-dependent exchange-correlation potential, although this limitation could, perhaps, be lifted. More general cluster methods have been developed, but have similar limitations.[9,10,18] By their nature, such full MS methods do not provide information about individual paths, and are thus of limited applicability for quantitative structural analysis. Another approach calculates full MS for all n-atom sets within a cluster,[19] and a hybrid approach has been suggested to merge EXAFS and XANES calculations.[20] We have also found that an accurate treatment of the embedded atomic-background absorption $\mu_0(E)$ is an important factor in near-edge calculations,[3] and is partly responsible for the present lack of quantitative agreement between theory and experiment in XANES. Our study adds to the pioneering treatment of Lee and Pendry,[1] in that we take the MS series to convergence, and also extend it for polarized XAFS and XANES calculations over the full experimental energy range, typically from threshold to 1500 eV. Compared to full MS techniques, path methods have a number of advantages. They simplify the inclusion of self-energy, core hole, and vibrational effects, permit the treatment of aperiodic geometries, and simplify XAFS analysis. Their major disadvantage is the numerical complexity of enumerating and calculating enough paths to converge the calculations.

Convergence of the MS path expansion is important for the utility of such calculations in structural analysis. Fortunately, there are two mechanisms that foster convergence. The first are the XAFS decay terms, i.e., the mean-free-path term and DW factors, which effectively limit the maximum path length that must be considered. The second mechanism is the approximate cancellation of all but a few dominant paths. This surprising result arises because the contributions from the myriad of weak MS paths act like random-phase noise. Since it is not *a priori* obvious which MS paths are most important, we have developed a constructive algorithm to enumerate paths and efficient path filters to discard the overwhelming majority that are insignificant. Accurate calculations of the remaining important paths are carried out using the Rehr-Albers (RA) scattering-matrix algorithm.[21] This approach is implemented in automated *ab initio* codes that are sufficiently accurate, portable, and easy to use, to serve as theoretical standards for general MS XAFS analysis. The codes are generalizations of our *ab initio* single-scattering XAFS code FEFF (version 3).[22–25] FEFF (version 5) includes MS paths in clusters with improved relativistic muffin-tin potentials and MS DW factors, and FEFF (version 6) adds dipole matrix elements with general elliptical-polarization dependence and an absolute energy scale based on atomic calculations. MS XAFS analysis packages that make use of the phase and amplitude data in the FEFF codes have been developed independently. These include, for example, FEFFIT,[26] a part of the University of Washington analysis package UWXAFS (version 2), and EXAFSPAK,[27] an analysis package developed at Stanford Synchrotron Radiation Laboratory.

Several illustrative tests of the method are presented here. Calculations for metallic fcc Cu are compared to full MS band-structure calculations to test both our path-enumeration algorithm and the accuracy of the RA approach. Calculations based on our full *ab initio* codes are then compared to measurements of XAFS in Cu, Cd, and Pt to provide tests of overall accuracy of XAFS, polarized XAFS, and XANES calculations. These calculations also check the various approximations in the broadened one-electron theory of XAFS. Comparisons with experiment and on various complex materials have also been carried out by several groups.[28–33] Other applications of these methods include, for example, diffraction anomalous fine structure[34] and photoelectron diffraction.[35]

II. MS THEORY OF XAFS

A. MS expansion

In this section we summarize the main theoretical ingredients in our codes. Additional technical details are given in Appendix A and B, and in previous publications.[3,8,21,24,36] To simplify the treatment, we will assume that many-body effects not included in the self-energy can be taken into account with additional broadening. Thus, we consider only a one-electron calculation of photoabsorption given by the Fermi golden rule with the dipole approximation, i.e.,

$$\mu(E) = 4\pi^2\alpha\omega \sum_f |\langle c|\hat{\epsilon}\cdot\mathbf{r}|f\rangle|^2 \delta(E - E_f). \quad (1)$$

Here $\alpha \simeq 1/137$ is the fine-structure constant, ω is the x-ray energy (we use Hartree atomic units $e = m = \hbar = 1$), $E = \omega - E_c$ is the final-state photoelectron energy, $\hat{\epsilon}$ is the x-ray polarization vector, and the sum is over unoccupied final states $|f\rangle$ at energies $E = E_f$. In accordance with the final-state rule,[37] the final states are calculated in the presence of a fully relaxed core hole, while the core states $|c\rangle$ are calculated with the the initial-state Hamiltonian. Details concerning the potential are given in Sec. II C below.

The calculation of the absorption cross section can be expressed in terms of a MS path expansion of the full propagator G.[1] To see this, we first rewrite the result for the absorption coefficient as

$$\mu \simeq -\frac{1}{\pi}\mathrm{Im}\langle c|\hat{\epsilon}^*\cdot r\, G(r,r';E)\,\hat{\epsilon}\cdot r'|c\rangle\theta_c(E - E_F), \quad (2)$$

where $G = 1/(E - H + i\eta)$ is the one-particle Green's function, $H = H_0 + V$ is the one-particle Hamiltonian including the self-energy, E_F is the Fermi energy, $H_0 = -(1/2)\nabla^2 + V_{\mathrm{int}}$ is the Hamiltonian of a uniform system with lossy potential $V_{\mathrm{int}}(E)$, $\delta V = V - V_{\mathrm{int}}$ is the scattering potential, which is defined relative to the interstitial potential V_{int} so the perturbation is negligible outside

the muffin tins, and $\theta_c(E) = (1/\pi)\tan^{-1}[\Gamma_c/(E_F - E)]$ is approximated by an arctangent function to account for the core-hole lifetime. The MS expansion for XAFS (Ref. 1) is then obtained by iterating the Dyson equation $G = G^0 + G^0TG$ in terms of free propagators, $G^0 = 1/(E - H_0 + i\eta)$, and scattering t matrices, and solving exactly for the central atom $G^c = 1/(E - H_c + i\eta) = G^0 + G^0 t_0 G^c$, i.e.,

$$G = G^c + \sum_{i\neq 0} G^c t_i G^c + \sum_{i\neq j\ i,j\neq 0} G^c t_i G^0 t_j G^c + \cdots \equiv \sum_{\Gamma} G^{\Gamma}. \tag{3}$$

The first term represents the background and the following path amplitudes G^{Γ} are the contributions from SS, double scattering, ..., representing all MS paths Γ. In this expression every term begins and ends with G^c, no site is repeated twice in a row, and only the first and last t matrices exclude the origin. In this work we use a semirelativistic calculation of the partial-wave phase-shifts δ_l that appear in the t matrixes,[38] $t_l = \exp(i\delta_l)\sin(\delta_l)$. In the semirelativistic treatment,[39] all relativistic effects within the atomic sphere are included, except for spin-orbit terms. The end result looks like a nonrelativistic treatment of scattering in that the matrices G^c and G^0 have the normal angular momentum and site basis $|L\mathbf{R}\rangle = i^l j_l(kr_{\mathbf{R}})Y_L(\hat{\mathbf{r}}_{\mathbf{R}})$, where $L = (l, m)$, $\mathbf{r}_{\mathbf{R}} = \mathbf{r} - \mathbf{R}$, j_l is a spherical Bessel function, and Y_L is a spherical harmonic.

There are two major computational bottlenecks in computing G. The first lies in the matrix multiplications $G^0tG^0\cdots$. For EXAFS, $l_{\max} = k_{\max}r_{\mathrm{mt}} \cong 15$ to 25, where k is the wave number (typically $k_{\max} \leq 20$) and $r_{\mathrm{mt}} \sim 1$ Å is the muffin-tin radius. This implies propagator-matrix $G^0_{L\mathbf{R},L'\mathbf{R}'} \equiv \langle L\mathbf{R}|G^0|L'\mathbf{R}'\rangle$ dimensions $N\bar{L} \times N\bar{L}$ where N is the number of atoms in the cluster and $\bar{L} = l_{\max}(2l_{\max} + 1) \cong 450 - 1200$, a size which generally limits exact methods to the near-edge region and to low-order (e.g., triple) scattering.[12] In carrying out the expansion, the central atom phase shifts are factored out, using the identity $\langle L\mathbf{0}|G^c|L'\mathbf{R}\rangle = \exp(i\delta_l)\langle L\mathbf{0}|G^0|L'\mathbf{R}\rangle$, $(\mathbf{R} \neq \mathbf{0})$. The second bottleneck is the sum over all scattering paths. Because the number of terms increases exponentially with distance, the calculations become impractical without some way to eliminate most paths.

The computational bottleneck of large propagator dimensions has been solved using the RA separable propagators.[21] In this method, the expression for G in terms of free propagators is replaced by a product of matrix scattering factors at each scattering site; these are obtained by expanding the free propagators as $G^0_{L\mathbf{0},L'\mathbf{R}} = [\exp(ikR)/kR]\Sigma_\lambda \tilde{Y}_{L,\lambda}Y_{L',\lambda}$, where λ (not to be confused with the mean free path) denotes the RA expansion indices (μ, ν). In practice the separable expansion converges rapidly, as the generalized spherical harmonic expansion factors scale as $Y_{L,\lambda} \sim (kR)^{-\lambda}$, leading to scattering factors of dimension at most 6×6 at all relevant energies. We have confirmed that the 6×6 matrices converge the path amplitudes to a typical accuracy of 1% over the range $0 < k < 20$ Å^{-1}, a figure usually smaller than experimental precision in XAFS. Although errors as large as 12% have sometimes been seen at very high energies in convoluted paths with large scattering angles, such "open" paths generally have negligible amplitudes. Thus Fritzsche's criticism[40] that the RA method can lose accuracy at high energies does not appear to be a disadvantage in practice. Moreover, it is straightforward to increase the matrix dimensions beyond 6×6 to increase accuracy and still achieve significant efficiency compared with other methods.

The effects of polarization in XAFS have been discussed previously[41] but they can naturally be included within the RA formalism (Appendix B). In our treatment, the RA approach permits a separation between the matrix element and the MS path scattering factors applicable for all edges, and also includes general elliptical polarization. Moreover, this treatment provides a basis for further developments such as circular magnetic dichroism and relativistic calculations including higher multipole couplings. Such polarization effects are conveniently expressed in terms of a polarization tensor; for general elliptical polarization,

$$\mu(E) = \mu_0(E)\left[1 + \sum_{\alpha\beta}(\epsilon_\alpha)^*\epsilon_\beta\chi_{\alpha\beta}(E)\right]. \tag{4}$$

Here μ_0 is independent of polarization, as the central atom scattering potential is assumed to be spherically symmetric, $\hat{\epsilon}$ is the (generally complex) x-ray polarization vector, and $\chi_{\alpha\beta} = \Sigma_\Gamma \chi^\Gamma_{\alpha\beta}$ is the XAFS tensor, which is obtained from the MS expansion. Within the RA formalism, the tensor dependence only appears in a "termination matrix" $M_{\alpha\beta}$ at the absorption site (see Appendix B), and one obtains for an n-leg path,

$$\chi^\Gamma_{\alpha\beta}(p) = \mathrm{Im}\, S_0^2 \frac{e^{i(\rho_1+\rho_2+\cdots\rho_n+2\delta_1)}}{\rho_1\rho_2\cdots\rho_n} \times \mathrm{Tr}_\lambda M_{\alpha\beta}F^{n-1}\cdots F^2F^1e^{-2\sigma^2_\Gamma p^2}, \tag{5}$$

where the trace is over the indices λ of the separable approximation and the indices λ, λ' in F and $M_{\alpha,\beta}$ are suppressed.[21] Here $\rho_i = p|\mathbf{R}_i - \mathbf{R}_{i-1}|$, $p = \sqrt{2(E - V_{\mathrm{mt}})}$ is the photoelectron momentum, and $F^i_{\lambda,\lambda'} = \sum_l t_l Y_{L,\lambda}\tilde{Y}_{L,\lambda'}$ is a scattering matrix (the analog of a scattering amplitude) at site i. Because the coupling to the core hole only appears in the matrix $M_{\alpha,\beta}$, it is fairly straightforward within the RA formalism to add quadrupole and higher-order couplings or to adapt the code to other spectroscopies. The polarization average XAFS (Ref. 21) is obtained by replacing $M_{\alpha,\beta}$ with $M = \Sigma_\alpha M_{\alpha,\alpha}/3$.

From Eq. (5) and Appendix B, each path Γ yields a contribution to the XAFS, which can be expressed in a form analogous to the standard XAFS equation,[21,23,42] but which now includes all MS and curved-wave effects,

$$\chi^{\Gamma}(k) = \sum_{\Gamma} \frac{S_0^2}{kR^2} |f_{\rm eff}^{\Gamma}(k)| \sin[2kR + \phi^{\Gamma}(k) + 2\delta_c(k)] \times e^{-2\sigma_{\Gamma}^2 k^2} e^{-2R/\lambda(k)}. \quad (6)$$

Although this standard form does obscure the physics of Eq. (5), it simplifies the comparison of MS path amplitudes in the path filters (Appendix A) and provides a standard tabulation of XAFS data for each path similar to that in terms of XAFS phases and amplitudes introduced by Lee and Pendry.[1] Here k is the momentum of the photoelectron, $f_{\rm eff}^{\Gamma}$ is the effective scattering amplitude for that path, S_0^2 is an amplitude reduction factor to account for intrinsic losses and interference, $\phi^{\Gamma}(k)$ is the net scattering phase shift, $\delta_c(k)$ is the final-state phase shift at the central (absorbing) atom, and $\exp(-2k^2\sigma_{\Gamma}^2)$ is the path DW factor. We have introduced the *effective path length*, $R = r_{\rm tot}/2$, for consistency with the usual convention for SS XAFS and similarly $\sigma_{\Gamma}^2 = \langle(\delta R)^2\rangle$ is the mean-square variation in R. The quantity $\lambda(k)$, historically called the mean free path, refers to the decay of the photoelectron wave-function amplitude and is roughly twice the decay length λ_L of electron beam intensities as measured by low-energy electron diffraction. Including the effect of the core-hole lifetime, $1/\lambda = 2/\lambda_L + 1/\lambda_c$. In our work these losses are taken into account by the imaginary parts of the photoelectron self-energy and the core-hole width, which give rise to a complex momentum: $1/\lambda = \mathrm{Im}\, p$.[22] The atomic core-hole lifetimes used in FEFF are interpolated from data in Keski-Rahkonen and Krause.[43] Details of our calculation of the background absorption $\mu_0(E)$ are discussed in a recent paper.[3] Briefly, the formula for μ_0 is the same as Eq. (1), but with final spinor states given by the radial semirelativistic Dirac equation. The upper component contains the embedded-atom wave functions $(1/r)R_0(r)Y_{lm}(\hat{r})$ calculated at energy $E = (1/2)p^2$. The appropriately normalized radial wave functions $R_0(r)$ are then obtained by matching the regular solution of the radial Dirac equation to the asymptotic behavior $R_0(r) = pr[j_l(pr)\cos\delta_l - n_l(pr)\sin\delta_l]$, $(r \geq R_{\rm mt})$, where j_l and n_l are spherical Bessel functions, δ_l is the lth partial wave phase shift, and the final-state l values are fixed by dipole selection rules. We have found that high numerical precision is needed in this calculation, and that a somewhat smaller grid size than that normally used in FEFF ($\delta r/r = 0.05$) is sometimes desirable at the highest energies ($E \sim 1500$ eV). The above matching procedure is equivalent to a calculation of the Jost function $F_l(E)$ (apart from a constant factor), which guarantees final-state normalization, as discussed by Holland *et al.*[4] and by Newton.[44] In particular, Holland *et al.* showed that the atomic cross section can be written as $\tilde{\mu}_0/|F_l|^2$, where $\tilde{\mu}_0$ is a reduced matrix element, which varies smoothly with energy.

B. Path enumeration

Path enumeration and filtering is based on a constructive algorithm that builds a list of all possible MS paths, in order of total path length $r_{\rm tot}$ out to a given cutoff $2R_{\rm max}$. Our algorithm uses a "heap"[45,46] to order the paths as construction takes place, and counts and eliminates degeneracies due to various symmetries using a "hash" sort;[45] these procedures are adapted from standard sorting algorithms.[46] This procedure is in contrast to other XAFS work, which typically enumerates paths based on the order of scattering (i.e., SS, double scattering, etc.). Below, we give an overview of the path enumeration scheme; technical details are given in Appendix A.

The exponential proliferation of paths with increasing path length is not surprising in that there are at least Z ways to add another leg to any path, where Z is the coordination number. Thus, there are of order $N(R) \sim Z^{2R/R_1}$ paths with effective path length R, where R_1 is the near-neighbor distance. This relation was verified by enumerating all paths with $R \leq 4R_1$ for fcc, bcc, and diamond structures. As noted above, we have found that the contribution of most MS paths can be neglected. Since the scattering phase shift $\phi(k)$ varies widely from path to path, the contributions from the numerous paths of small amplitude and the same length add like random-phase noise. For N paths, all with about the same amplitude $|\chi_{\Gamma}|$, the total amplitude is thus $|\chi| = |\sum_{\Gamma}\chi_{\Gamma}| \sim |\chi_{\Gamma}|\sqrt{N}$. The net result is that the uncounted paths contribute a small fluctuating signal, which is usually negligible.

The plane-wave scattering amplitude $f(\beta)$, where β is the scattering angle, can be used to obtain a rough estimate of the importance of a given path. This amplitude is largest for forward scattering and has a smaller maximum for back scattering.[1] In the plane-wave approximation (PWA), the MS path amplitude for a n-leg path is

$$|\chi_{\rm pw}^{\Gamma}(p)| \sim \frac{\cos(\beta_0)}{\rho_n} \prod_{i=1}^{n-1} \left| \frac{f(\beta_i)}{\rho_i} \right| e^{-2R/\lambda}, \quad (7)$$

where β_i is the scattering angle at site i, i.e., $\cos(\beta_i) = \hat{R}_i \cdot \hat{R}_{i+1}$, and $\beta_0 \equiv \beta_n$. DW factors do not change the order of magnitude of the path amplitudes and are ignored. From Eq. (7), we see that the mean amplitude for a n-leg path $|\chi^{(n)}|$ is given by

$$|\bar{\chi}^{(n)}| = \frac{1}{p\bar{f}} \left(\frac{\bar{f} e^{-R_1/\lambda}}{R_1} \right)^n Z^{n/2}, \quad (8)$$

where $\bar{f}$ is an appropriate average of $f(\beta)$ over scattering angles and the factor $Z^{n/2}$ assumes random-phase averaging. Thus, convergence is geometric in the typical path-leg amplitude $\bar{f}e^{-R_1/\lambda}/R_1$. The effect of vibrations and disorder also limits the range to R of order $R_1/\sigma k$, where σ is the rms fluctuation in bond length. This is due to the decoherence of the signal when the phase error $nk\sigma > \pi$, where $n \sim 2R/R_1$ is the number of scatterers. This effect especially aids convergence of high-order MS paths. Comparing $|\bar{\chi}^{\Gamma}|$ of all the paths with $R \geq 3R_1$ to the first SS path amplitude $|\bar{\chi}^{(1)}|$ in Cu, we find that the random-phase noise term from the neglected paths is only about 0.4% of $|\bar{\chi}^{(1)}|$, well below the typical experimental

precision of a few percent.

We now briefly describe the path filters introduced in the code to remove negligible paths. Paths are eliminated at four places in the calculation: (a) during path construction; (b) after construction but before degeneracy checks; (c) after the path list is complete using the PWA estimate and degeneracy checks; and (d) after a full curved-wave calculation on the surviving paths with full degeneracy checks. Eliminating paths earlier improves efficiency, but the filters (a) and (b) can have large errors and must be used conservatively. The last two filters (c) and (d) are more accurate but require more computation. In practice, these last two filters $C_{\rm pw}$ and $C_{\rm cw}$ alone are adequate to filter all paths through the third SS distance. In the remainder of this paper, we will refer explicitly to $C_{\rm pw}$ and $C_{\rm cw}$ [see Eq. (A3)], which are defined as the mean-path amplitudes, including degeneracies, expressed as a percentage of the first near-neighbor path amplitude. In related work on polarization-dependent XAFS calculations,[41] Binsted and Norman used importance filters based on peak amplitudes. However we have found that the precise form of the filter is not important. We have also found that this path-finder algorithm is adequate for XAFS calculations in all materials we have tested to within 15 eV of the absorption edge, and for most of these even closer to the edge. In a few cases, particularly low-Z absorbers with small core-hole lifetimes, more paths or more sophisticated path filters may be needed to describe XANES accurately.

C. Potentials and Debye-Waller factors

Our final-state scattering potential is calculated with a generalization to clusters of the same method that was used in our earlier code FEFF3,[22–24] so we only briefly review the procedure here. The code first calculates the potential for each free atom using a relativistic Dirac-Fock-Slater atom code[47] with local von Barth–Hedin exchange, and then uses the Mattheiss prescription[48] to overlap the free atom charge densities and hence construct spherical muffin-tin potentials.[38] This approximation has been found to give a good approximation to self-consistent potentials and is fully adequate at EXAFS energies. However, chemical effects and muffin-tin corrections may be important in the near-edge region. Muffin-tin radii are determined automatically using the Norman prescription, and interstitial potentials and densities are determined by averaging these quantities outside the muffin-tin spheres. The potential also includes an energy-dependent self-energy, which is usually taken to be the local Hedin-Lundqvist plasmon-pole model plus a correction due to Quinn[49] to account for low-energy electron-hole losses. We use an analytical expression for the imaginary part and a fast polynomial fit for the real part of the self-energy.[22] This factor is essential to describe the energy-dependent losses and energy shifts observed in experimental spectra. Our algorithm builds in overall charge neutrality and has been automated to the extent that the only inputs necessary are the atomic numbers of the atoms in the cluster and their positions. The semirelativistic phase shifts used in our work are calculated using a method discussed by Loucks[38] for $0 \le l \le 24$ over a k range from 0 to 20 Å^{-1}.

Single-scattering XAFS DW factors have been calculated in several cases[50] or can be be obtained from a fit to the data, e.g., from experiments done at several temperatures.[2] For MS, the problem is more difficult due to the displacement-displacement correlations between sites, and thus each path has its own DW factor. For simplicity, we neglect here the usually small curved-wave effects[51] on DW factors as well as angular and anharmonic effects, which require higher-order cumulants.[52,53] Expanding the effective path length to linear order in the fluctuation $\mathbf{u}_i$ at site i, we obtain

$$\sigma_\Gamma^2 = \frac{1}{4}\sum_{ij}\langle(\mathbf{u}_i - \mathbf{u}_{i'})\cdot\hat{\mathbf{R}}_{ii'}(\mathbf{u}_j - \mathbf{u}_{j'})\cdot\hat{\mathbf{R}}_{jj'}\rangle, \qquad (9)$$

where $\mathbf{R}_{ij} = \mathbf{R}_i - \mathbf{R}_j$, $i' = i+1$, $j' = j+1$. In our work the displacement-displacement correlation functions are approximated using an isotropic Debye model:[50,52,54]

$$\begin{aligned}\langle u_{i\alpha}u_{j\alpha}\rangle &= \frac{\hbar}{\sqrt{M_iM_jN}}\sum_{\mathbf{k}}\frac{\coth(\beta\hbar\omega_k/2)}{2\omega_k}e^{i\mathbf{k}\cdot(\mathbf{R}_i-\mathbf{R}_j)} \\ &= \frac{3kT}{\omega_D^2\sqrt{M_iM_j}}\int_0^1 dw\, y\coth(wy/2)\frac{\sin(wx)}{x},\end{aligned} \qquad (10)$$

where $x = k_DR_{ij}$, $y = \hbar\omega_D/kT = \theta_D/T$, w is a dimensionless frequency variable, θ_D is the Debye temperature, $k_D = (6\pi^2N/V)$, N/V is the inverse of the average volume per atom (obtained in terms of the calculated Norman radii), and M_i and M_j are the atomic masses at sites i and j in amu. The integrations are performed using a modified Romberg-Simpson algorithm. This correlated Debye model turns out to be quite good for linear paths (typically the most important ones) in homogeneous materials. However, this method ignores angular correlations that may be important in some systems.

III. COMPARISON WITH FULL MS THEORY

In this section, we compare the results of our approach to a broadened band-structure calculation for Cu. Independent comparisons with other full MS methods have been made by Dagg *et al.*[28] The band-structure results were obtained using the linear augmented plane wave (LAPW) method[14] over an energy range from threshold to 15 Ry ($0 \le k \le 7$ Å^{-1}).[14,17] To avoid ambiguity, our calculations used exactly the same self-consistent-field results (SCF) potentials and scattering phase shifts.[14] Subsequently, the raw band-structure results were Lorentzian broadened to simulate inelastic losses and monochromator resolution; our MS results were broadened equivalently, by adding a constant imaginary part of 4 eV (half-width) to the potential. This value corresponds to that for the observed λ in Cu over the energy range being studied.[22] The band-structure technique cannot include the effect of the core hole on the absorbing atom's potential without the use of a super cell, nor can correlated

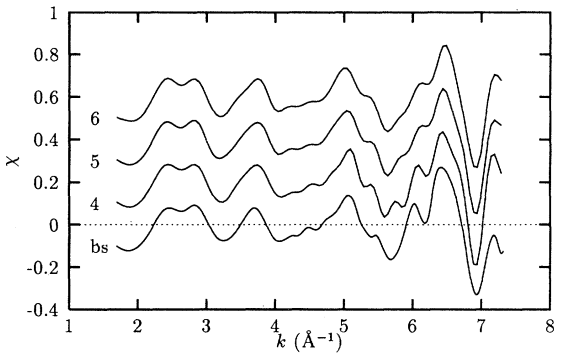

FIG. 1. Band structure (BS) and FEFF MS calculations of Cu XAFS including paths up to the 31st shell (see text); the labels indicate the curved-wave filter values C_{cw} in %.

DW factors be included properly. Although these effects are important in the comparison of theory and experiment, they can be ignored for the purpose of testing the convergence of the MS expansion.

For convergence, the MS calculation must consider all paths with $R < R_{max} \sim \lambda$, where the mean λ is of order 12 Å. Thus, the 31st shell in Cu at 12.78 Å is a convenient upper limit. From the relation $N \sim Z^{2R/R_1}$, we expect about 6×10^{10} paths with a typical cubic degeneracy of 48, or about 1.2×10^{9} unique paths. We began the calculation with 8874 unique paths representing all 434 546 distinct paths with $R \leq 8.47$ Å, the distance to the 12th shell. Although time consuming, this calculation can be done, e.g., in a few CPU hours on a SUN SPARC, and the XAFS spectrum from various subsets of paths can be compared to the total. The rms error in the broadened LAPW Cu band-structure calculation is $\epsilon_{bs} = 0.038$ and is due primarily to the differences in the linearized phase shifts and basis sets used in the various energy panels. This corresponds to a C_{cw} filter of about 6% yielding only 30 paths. Tightening this filter to 3% increases the number of paths that must be retained to 60, and decreases the estimated rms error in the calculation from 0.0153 to 0.0139.

Knowing that the final curved-wave filter can safely be set to $C_{cw} \simeq 4\%$, our MS calculation was extended to the 31st shell distance and all four path filters were used. After studying the convergence as the final filter parameters were varied, the values C_{cw} and C_{pw} were set to 4% and 1.25%, respectively, with the result that only 56 paths through the 31st shell distance were retained. Several checks were made using a more conservative set of filters and 9684 trial paths, but all yielded the same 56

TABLE I. The 24 most important MS paths in Cu (R_1=2.56 Å) through shell 6. Here R is the effective path length; C_{cw} is the importance in percent of each path relative to the first SS path; the path labels follow the notation of Lee and Pendry (Ref. 1), where leg lengths are denoted by neighbor distances; i.e., "1" denotes a nearest-neighbor path with length R_1, "2" the second-neighbor distance R_2, etc. The degeneracy N_Γ is the number of equivalent paths; n indicates the number of legs for each path; and path types include "SS" single scattering, "focusing" paths with only forward-scattering events except for one back-scattering, and "linear" collinear paths with more than one back-scattering event.

Path	R	C_{cw}	Label	N_Γ	n	Type
1	2.56	100.00	11	12	2	SS, first shell
2	3.61	20.23	22	6	2	SS, second shell
3	3.83	12.28	111	48	3	triangular
4	4.36	8.96	211	48	3	triangular
5	4.43	44.77	33	24	2	SS, third shell
6	4.77	13.47	311	96	3	triangular
7	4.77	6.99	131	48	3	triangular
8	5.11	14.32	44	12	2	SS, fourth shell
9	5.11	32.63	411	24	3	focusing
10	5.11	7.17	141	12	3	linear
11	5.11	4.04	1111	48	4	dogleg
12	5.11	24.16	1111	12	4	focusing
13	5.11	8.74	1111	12	4	linear
14	5.30	4.02	321	48	3	triangular
15	5.30	4.55	312	48	3	triangular
16	5.71	6.15	313	48	3	triangular
17	5.72	19.93	55	24	2	SS, fifth shell
18	5.94	4.83	512	48	3	triangular
19	5.94	5.31	251	48	3	triangular
20	6.05	4.83	431	96	3	triangular
21	6.05	6.36	413	96	3	triangular
22	6.05	7.70	3111	96	4	partly focusing
23	6.05	6.02	1311	96	4	partly focusing
24	6.26	4.89	66	8	2	SS, sixth shell

paths. In particular, there were no paths with R greater than the 23rd shell distance $R = 11.11$ Å confirming that R_{max} was chosen large enough. Fig. 1 compares our MS calculations to the middle panel Cu band-structure result as the filter C_{cw} is varied to illustrate convergence. Note that the features in the band-structure calculation are correctly modeled in amplitude, shape, and in location in k. The discrepancies that do exist are likely dominated by the limited (3.8%) accuracy of the band-structure calculation as noted above.

It is interesting to examine these 56 paths to find out which factors make a path important. A representative list of the 24 most important paths out to the sixth shell distance 6.26 Å is given in Table I, and a summary of the important paths, classified according to type, is given in Table II. The importance of SS and focusing paths is confirmed. Surprisingly, we have found that triangular paths can be nearly as important as focusing paths. The longest of the 56 paths is the SS contribution from the 22nd and 23rd shells and has degeneracy of 72. The longest MS path with significant amplitude has $R = 10.22$ Å; it is a seven-legged linear path with five forward scatterings to an atom in the 17th shell, a degeneracy of 24, and an amplitude about four times that from SS from the 17th shell. The longest nonlinear path is a triangle with exterior angles of 175°, 20° and 165° (almost forward scattering). For this path, $R = 9.9$ Å and $C_{cw} = 8.0\%$. The longest open triangular path has $R = 6.9$ Å and $C_{cw} = 9.5\%$.

On the basis of this path study, we find that (1) the mean free path λ (about 12 Å at $k = 7$ Å^{-1}) is an approximate upper limit to the maximum effective path length R_{max} that must be considered; (2) the order of the scattering is not a good measure of importance. Some six- and seven-legged paths have significant amplitude and some SS paths do not; (3) as expected from the shape of $f(\beta)$, forward-scattering events amplify the XAFS and are usually important. Many other "linear" or "focusing" paths also have significant amplitude. Back-scattering events do not amplify, but they have larger scattering amplitudes than those at intermediate angles. Also, some linear paths with several back-scattering events are important. The dominance of forward scattering[1] in the fourth shell of Cu is confirmed; (4) many triangular paths are important. For example, the first triangular path (an equilateral triangle with leg length R_1) is essential for an accurate calculation of the second shell. This result is particularly important in close-packed materials.

These findings suggest a "minimal MS" hypothesis of path importance, namely, that predominantly SS, focusing (i.e., linear and near-linear), and triangular paths are important for XAFS calculations. This hypothesis is consistent with the MS results of Lee and Pendry[1] up to the fifth shell in Cu, which suggested that except for shadowing paths, the effect of MS is generally smaller than SS. The hypothesis is an extension in that it stresses the more general importance of triangular paths at much longer distances in converged calculations. With this hypothesis, only five of the paths in Table II are left out, and the structure of the XAFS is essentially unchanged within the tolerance set by the path filters. If more generally valid, especially near the edge, this hypothesis can greatly simplify MS XAFS calculations and their interpretation. A more general hypothesis is desirable,[41] but we have occasionally encountered important paths that appear hard to predict.

We have also found that the main features of the XAFS and XANES spectrum of Cu in k space can be given a path interpretation. That is, like shape resonances, such features are largely the result of interference between several paths. The splitting in the double peak at $k = 2.5$ Å^{-1} is caused by two paths, SS from the third and seventh shells at 4.43 Å and 6.76 Å, respectively, due to a path-length "resonance" in R ($R_3 \cong 2 \times 2.2$ and $R_7 \cong 3 \times 2.2$ Å) that leads to constructive interference. The peaks at 3.7 and 5 Å^{-1} are due primarily to the contributions from SS paths from the first and third shells, at 2.556 and 4.427 Å, respectively. This is also due to interference from the effective path lengths $R_1 \cong 1 \times 2.5$ and $R_3 \cong 2 \times 2.5$ Å. The peculiar slowly rising edge just above threshold $k = 0$ can be regarded as a "blackline." The feature is actually a very large and negative XAFS amplitude due to constructive interference of SS paths R_1 and R_3, and results in a large *decrease* in intensity — just the opposite of that in a "whiteline." The fine wiggles in the spectrum near $k = 4.3$ Å^{-1} are caused by three paths of comparable amplitudes at $R = 7.67$ Å, the distance to the ninth and tenth shells. One of these paths is SS with degeneracy 36 and the other two are 5 leg forward-scattering paths with degeneracy 24. This result will be used in the comparison with experiment in Sec. IV A to demonstrate that the calculated mean free path is too short near $k = 4$ Å^{-1}; i.e., that our self-energy calculation has too much loss at intermediate energies. It also shows that MS signals at least through the tenth shell are clearly evident in experiment.

TABLE II. Cu path analysis: The 56 paths are sorted by type. A total importance $\Sigma|\chi^{\Gamma}_{cw}|$ is defined as the sum of the mean amplitudes $|\chi^{\Gamma}_{cw}|$ in each category, normalized to 100% and expressed in %. The line "all other paths" is the amplitude difference between the 56 path and a 1215 path calculation. The notation is the same as in Table I.

N	$\Sigma\|\chi^{\Gamma}_{cw}\|$ (%)	Type
15	46.19	SS
15	24.23	focusing
17	20.67	triangular
2	2.28	linear triangular
4	4.40	other linear
2	1.48	dogleg
1	.73	quadrilateral
1159	9.50	all others

IV. COMPARISON WITH EXPERIMENT

The theoretical study of the previous section gives confidence that the MS path expansion can converge with a few dozen paths, which can be enumerated efficiently. Now we compare such calculations with exper-

iment in Cu, Cd, and Pt. These materials were chosen because they are well characterized and all exhibit strong MS effects; thus, they are nontrivial cases for testing convergence of the MS expansion. In our preliminary treatment[5] we also discussed high-order MS calculations of the σ^* shape resonances[55] for N_2 and O_2. We showed that such continuum shape resonances are described quantitatively with about a dozen repeated back scatterings of the photoelectron, and we also gave a generalization of the "Natoli rule"[56] relating bond lengths with shape-resonance location.

A. fcc Cu

Cu metal has been a traditional test case for XAFS theory.[1,22] Here we compare our results to a recent experimental study with data taken at 10 K on a carefully annealed sample.[57] The background subtraction was carried out using the semiautomated background removal code AUTOBK,[33] with an energy-dependent background $\mu_0(E)$ and some hand-fitting near the edge. To avoid over emphasizing the low-energy end of the spectrum, the χ data are weighted by k^2. The calculation was done with a fixed 10-K lattice constant $a = 3.6032$ Å and included all important paths through the 23rd shell ($R = 11.11$ Å). Filtering with a cutoff $C_{cw} = 4\%$ yielded 105 paths. The correlated Debye model was used for DW factors, with Debye temperature Θ_D=315 K. The only free parameters in the fit are the amplitude reduction factor $S_0^2 = 0.912$ and an energy zero shift $E_0 = 5.1$ eV. Note that the fit to the data is extremely good over the entire k range, and also up to about 8 Å in R space (Fig. 2). Except for the parameters S_0^2 and E_0, this is the result of a completely automated *ab initio* calculation.

As the main application of the XAFS technique involves relatively short paths, a Fourier transformation to position space $\tilde{\chi}(R) = FT[k^2\chi(k)]$ can be used to isolate various contributions. Note that the peaks in $\tilde{\chi}(R)$ are broadened and shifted to smaller R. This effect is due primarily to the net scattering phase shift ϕ in the XAFS equation [see Eq. (6)] from the product of scattering amplitudes: MS paths are generally shifted more than SS, the shift typically being 0.3 Å – 0.4 Å per scatterer. Thus, to match the experiment through some distance R_{max}, MS paths with R greater than R_{max}, typically by 1 Å – 2 Å, must be considered. This also suggests that the use of phase-corrected XAFS Fourier transforms, i.e., phase shifted with theoretical phase factors $\exp[-i(2\delta_c + \phi^{(1)})]$, will yield much sharper peaks close to the correct SS distances that are superposed on a background of broad MS contributions.

As an example of interference between successive shells in the Fourier transform, consider the second shell in Cu (Fig. 3). In addition to SS paths and some leakage from the third shell, we have found that the first two triangular paths, the 111 equilateral triangle [the notation used here is described in Table I] and the 121 right triangle, are particularly important. Note that the Fourier transform (FT) of the 111 triangle path peaks at a smaller distance than that from the second SS path, even though the 111 path length is longer.

Since XAFS is often used as a distance probe, the error Δr in the near-neighbor distance estimate is of particular

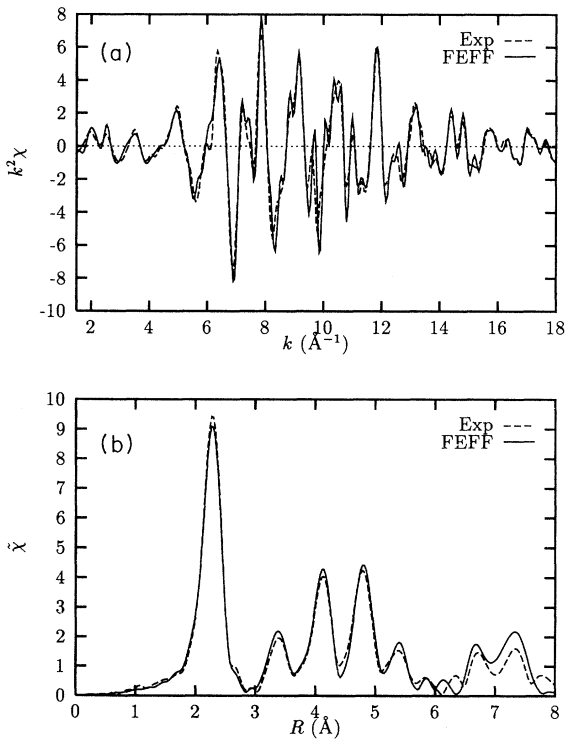

FIG. 2. Cu $k^2\chi(k)$ XAFS from experiment at 10 K and from FEFF calculations using 105 paths through the 23rd shell ($R = 11.11$ Å), $C_{cw} = 4\%$, $S_0^2 = 0.912$, an E_0 shift of 5.1 eV, and correlated Debye model DW factors (a) (upper panel) in k space, and (b) (lower panel) the Fourier transform of $k^2\chi$ over the range $2 \le k \le 18$ to R space, with Hanning windows of width 3 Å^{-1}.

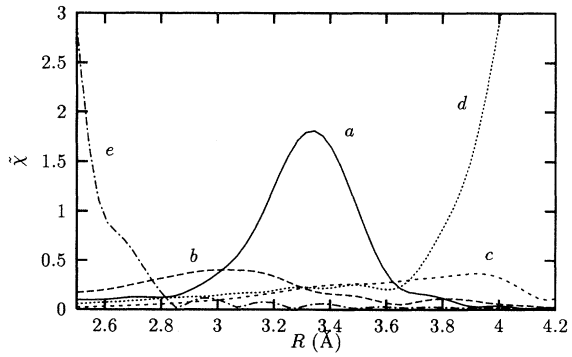

FIG. 3. Cu second shell XAFS Fourier transform over the range $2 \le k \le 18$ to R space, showing contributions from various paths (see text). (a) SS from second shell, $R = 3.60$ Å; (b) 111 triangle $R = 3.82$. (c) 121 right triangle, $R = 4.35$; (d) SS from third shell, $R = 4.41$; (e) SS from first shell, $R = 2.55$.

importance. The need for a new analysis for Cu was motivated by the large error $\Delta r = 0.018$ Å reported in our previous study,[22,23] in contrast to errors in Pt and $GeCl_4$ only a tenth as big. The fitting was done using a recently developed R-space XAFS analysis code FEFFIT,[26] an implementation of the Levenberg-Marquardt nonlinear least squares algorithm, which uses MS amplitudes and phases from FEFF. The data were fit through the fourth shell using the 12 most important paths, varying the lattice constant a, E_0, and S_0^2, and either using the correlated Debye model or fitting the DW factors independently. All fits were done with k between 2 and 18 $Å^{-1}$, k^2 weighting, and Hanning windows of width 3 $Å^{-1}$. The results of the two fits were the same within the statistical uncertainty of the fitting procedure, and gave $S_0^2 = 0.93$, $E_0 = 5.2$ eV, and an error in the lattice constant $\Delta r < 0.001$ Å,[36] thereby completely resolving the previous discrepancy. We have ignored small anharmonicity corrections at these temperatures, which for Cu can give errors of about this order of magnitude.

The correlated Debye model can also be tested with this data, though not with the accuracy of temperature-dependent measurements.[52] There are approximately $N_{\rm ind} = (2/\pi)\Delta k \Delta r \cong 32$ independent parameters in the experimental k range and a range in R of a few Å, enough to fit σ^2 for the 12 most important paths through the fourth shell. Fits through the second shell ($R = 3.60$ Å) and through the fourth shell ($R = 5.11$ Å) were done with the result that the calculated SS and linear path DW factors differ from the fit values by between 5 and 15%, including a McMaster correction of 0.0003 $Å^2$.[24] However, the calculated DW factor for the 111 triangle $\sigma^2 = 0.0035$ $Å^2$, is in error by about 85% with respect to the fit value of 0.0065 $Å^2$. We do not yet understand this large discrepancy; it may be due to the neglect of angular correlations,[58] residual disorder, or simply numerical interference with other important SS and MS paths at this distance.

An energy-dependent photoelectron self-energy has been found to be essential for accurate SS XAFS calculations,[22–24] as clearly seen in the overall XAFS phase. This quantity is the phase of the back transform, which is determined by Fourier filtering the first SS shell. The term $2kR_1$ was subtracted from the total phase of the back transformed χ, leaving only the total scattering phase shift $\phi(k) + 2\delta_c(k)$ (Fig. 4.) Note that the experimental phase falls between the Hedin-Lundqvist (HL) and Dirac-Hara (DH) self-energy models, suggesting the inadequacy of both. For XAFS analysis, the discrepancy between either model and the data can be nearly eliminated by an E_0 shift of a few eV. However, the HL model gives somewhat more accurate results to about 2 eV closer to the edge than the DH model.

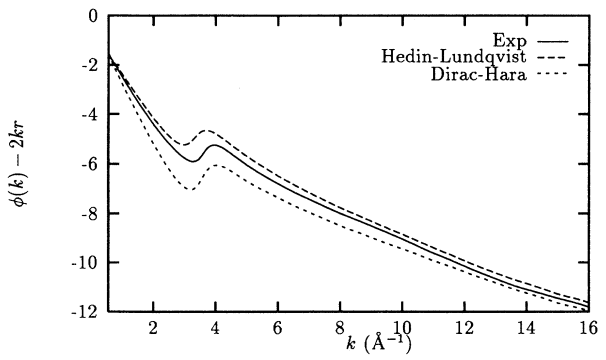

FIG. 4. First shell XAFS phase shifts $2\delta_c + \phi$ from the Hedin-Lundqvist (long dashes) and Dirac-Hara (short-dashes) self-energies, and from Fourier-filtered and back-transformed 10 K Cu experiment (long dashes).

The second important physical quantity obtained from the self-energy is the XAFS mean-free path λ. Although comparisons with calculations done by Penn[59] show that the HL model is reasonably accurate at high energies, the model appears to give too much loss at low energies. Consider the small high-frequency wiggles near $k = 4.3$ $Å^{-1}$ (Fig. 2). As indicated in Sec. III, this feature is caused by several paths at the combined ninth and tenth shell distance $R \simeq 7.64$ Å. With our HL λ, however, these features are almost completely washed out. Increasing the mean free path using a 2-eV reduction in the imaginary part of the self-energy is enough to bring back the contribution from these paths. A possible source of the error is the free-electron treatment of core-electron contributions to the HL model. Our calculations also indicate that the HL model is accurate beyond the near-neighbor distance, a region untested in our previous study.

B. Polarized hcp Cd XAFS

Extending the FEFF code to include general elliptical polarization using the RA formalism has now made it possible to carry polarized MS XAFS calculations to convergence in arbitrary materials. Our treatment of polarization [Appendix B] differs from other approaches[41] in that the curved-wave polarization tensor is lumped into a single matrix factor for all absorption shells. Also, our approach enumerates and takes advantage of the symmetries implied by the polarization dependence.

As an example of polarization-dependent XAFS, we have calculated the spectra for $\hat{\epsilon}$ along the a and c axes of hcp Cd. The calculations used 178 paths out to $R = 8.0$ Å. The XAFS signal differs between a and c polarizations because the near-neighbor bond lengths in the distorted hcp structure differ by 0.28 Å. The calculated result for a-axis polarization using a Debye temperature fit to 170 K, is compared to the experimental data of Tyliszczak *et al.*[60,61] in Fig. 5(a). The experimental data were derived from Cd K shell XAFS recorded in transmission at 11 K from a thin single crystal. Overall the agreement between calculation and experiment is satisfactory, though usually less so than for polarization average measurements. The discrepancies are believed to be due to sample distortion and possibly some misalignment, both factors leading to a mixture of polarizations and hence interference between XAFS signals from slightly different lattice constants. Since alignment of $\hat{\epsilon} \parallel$ the c axis actually samples both the shorter in-plane Cd-Cd distance

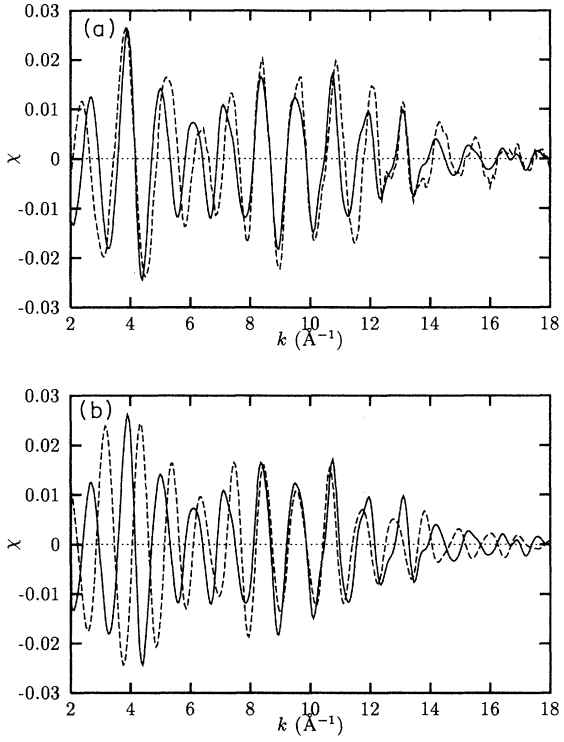

FIG. 5. (a) (upper panel) Cd XAFS signal $\chi(k)$ for a-axis polarization from experiment at 11 K (dashes) and from FEFF calculations (solid) using 178 paths with $R \leq 8$ Å, $S_0^2 = 0.9$, and correlated Debye model DW factors; (b) (lower panel) comparison between theoretical calculations of Cd XAFS $\chi(k)$ for a-axis (solid) and c-axis (dashes) polarization.

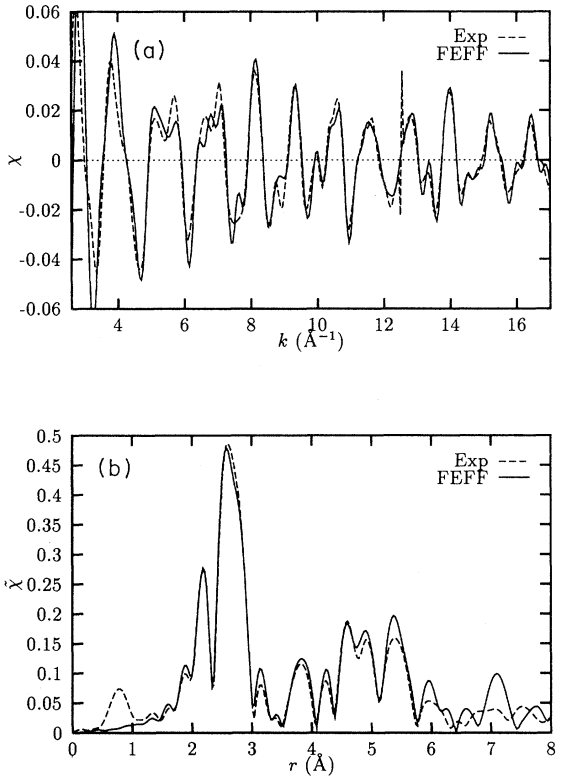

FIG. 6. Pt $k\chi(k)$ XAFS from experiment at 80 K and from FEFF calculations using 85 paths through the 12th shell (R = 9.18 Å), C_{cw} = 4%, $S_0^2 = 0.84$, an E_0 shift of 6.3 eV, and correlated Debye model DW factors. (a) (upper panel) in k space and (b)(lower panel) the Fourier transform of $k\chi$ over the range $3.5 \leq k \leq 15.6$ to R space, with Hanning windows of width 3 Å^{-1}.

and the longer out of plane Cd-Cd distance, the $\hat{\epsilon} \parallel c$-axis data will always be less "sharp" than $\hat{\epsilon} \parallel a$-axis data. Theoretical calculations of these differences are shown in Fig. 5(b). Because of these effects, polarized XAFS experiments are more difficult than polarization-averaged experiments and less accurate, but have the advantage of providing important orientational information. Additional polarization-dependent calculations using FEFF6 have been carried out for surface systems.[62,63]

C. fcc Pt XAFS and XANES

Pt is another important test case due to its complex inner-shell structure and the large k range of the signal. We have shown previously that relativistic phase shifts used in FEFF give an excellent description of the SS XAFS.[24] Here we present theoretical MS calculations both of the XAFS and XANES.

Figure 6 shows the polarization-averaged XAFS spectrum, both as calculated and measured experimentally. The experimental data used for this comparison was collected for a Pt foil at 80 K.[64] The background subtraction was done using AUTOBK.[33] Due to the whiteline in Pt, the amplitude of the background below about $k = 3.5$ Å^{-1} is not well defined, so XAFS data below 3.5 Å^{-1} were not used and the data were weighted by k to avoid overemphasizing the low-energy spectrum. The calculation was carried out through the 12th shell (R = 9.18 Å), and filtering with C_{cw} = 4% yielded 85 paths. The correlated Debye model was used for the MS DW factors with Debye temperature Θ_D=230 K. The only free parameters in the fit were $S_0^2 = 0.84$ and $\Delta E_0 = 6.33$ eV, and the trial 80-K lattice constant was set to $a = 3.9162$. The calculation and the data are found to agree within a few percent over the entire k range and through about $R = 6$ Å in r space (Fig. 6). The statistical error in the lattice constant is less than 0.001 Å, determined by fits to the first shell only and by fitting through the fourth SS shell and allowing a, S_0^2, and E_0 to vary. The correlated Debye model was again tested, and the theoretical value $\sigma^2 = 0.0019$ Å^2 agreed with the fit to within 20%. The fit for the second SS shell $\sigma^2 = 0.0023$ Å^2 gave a discrepancy of 12%, much smaller than the corresponding discrepancy found for Cu.

Pt metal also provides an important test case for XANES calculations. The XANES spectrum is interesting, since it features a strong whiteline at threshold (Fig. 7). This spectrum is obtained from the relation $\mu = \mu_0(1+\chi)$, where μ_0 is the background absorption and χ is the polarization averaged XAFS. Note that the theo-

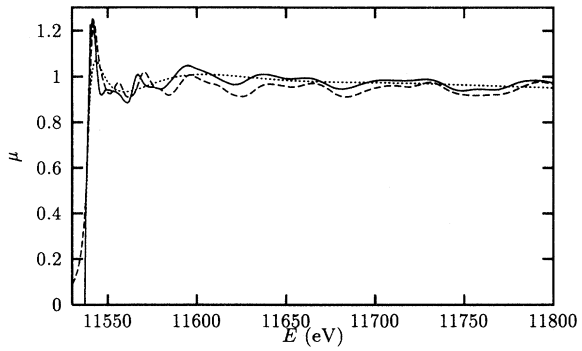

FIG. 7. Normalized Pt XANES μ from experiment (solid) and from FEFF (long dashes) with the same parameters as in Fig. 6. The theoretical background absorption function μ_0 from FEFF is also shown (short dashes).

retical XANES structure is in reasonable agreement with experiment. In particular the whiteline is adequately reproduced by the theory. Moreover, the theory correctly accounts for all the peaks in the experimental spectrum, except for slight errors in peak locations and amplitudes. We believe the discrepancy at low energies is largely due to the inadequacy both of our self-energy model and the calculation of the atomic background. The discrepancy just at threshold indicates that the approximation of the edge by a simple arctangent function is not adequate when the edge is dominated by a whiteline. Strikingly, we have found that the presence of a full corehole is a crucial ingredient in the calculations. A comparison of μ_0 calculated with and without a corehole shows that the initial-state configuration gives much too strong a whiteline. This result lends support to the final-state rule[37] and suggests that band-structure calculations that ignore the core hole are inadequate to describe whitelines quantitatively. The nonmonotonic behavior in $\mu_0(E)$ beyond the whiteline also illustrates the importance of atomic XAFS.[3] Though we cannot distinguish multielectron excitations[65] from such atomic effects, multielectron effects in the experiment cannot be significantly larger in magnitude than the background variation effect observed here. In these calculations, the Fermi energy was 2 eV too high, and an additional 2 eV was added to the estimate of core-hole lifetime of 4.8 eV to account for instrumental resolution. The experimental $L_{\rm III}$ threshold energy of 11564 eV indicates that the absolute energy scale based on a relativistic atomic total energy calculation (and ignoring extra-atomic relaxation), which gives a threshold at 11542 eV, is off by about 20 eV.

V. CONCLUSIONS

We have shown that high-order MS XAFS and XANES calculations to full MS accuracy can be achieved for several closed-packed materials with large MS effects. For these cases and many others,[28–33] the MS expansion converges to within typical experimental precision of a few percent with of order 100 paths. The algorithm has been implemented in an automated code FEFF, which makes possible XAFS studies going well beyond the first coordination shell. The increase in range also permits a test of models of the photoelectron self-energy, MS DW factors, and features of the theory. Thus, while problems still exist at and below the edge, we feel the problem of calculating MS in continuum XAFS can be generally regarded as solved, apart from the effects of disorder.

The XAFS lore concerning MS has been critically addressed. The typical value of the XAFS mean free path is found to give an effective maximum path length. Although the importance of forward scattering is confirmed, triangular paths can also be "important." The order of the scattering is not necessarily significant; high-order MS paths are usually important only when paths contain focusing scatterers. These observations have led to a "minimal MS hypothesis" of MS path importance, namely, that the most important paths are single-scattering, focusing, linear (or nearly so), and triangular. Almost all other paths can be neglected. This conclusion is only apparently in contrast to an earlier assessment of MS path importance based on weaker importance criteria.[11] We have also found that MS DW factors play an important role in converging the MS expansion, and that full MS calculations that ignore correlated DW factors can overestimate the XAFS.

The theoretical XAFS agrees well with experiment, even beyond the first shell, showing that the physical parameters used in FEFF are accurate enough to define theoretical standards for MS XAFS analysis. Distance errors in the materials tested are of order of a few 0.001 Å, comparable to errors in x-ray diffraction studies. The agreement in the XANES region is less satisfactory; although the structure is qualitatively correct, discrepancies in peak positions and heights are evident, indicating the need to improve the calculations.

A broadened one-electron theory is found to give a good description of experiment in the materials studied here. Multielectron effects and other many-body effects are either small, or can be lumped into phenomenological broadening factors. The overlapping atom potentials and the spherical muffin-tin approximation appear to be adequate for EXAFS calculations, but may require improvements near the edge. The Hedin-Lundqvist photoelectron self-energy calculation is generally adequate for XAFS use, as shown both by phase studies and by the small errors in determinations of the lattice constant. However, the mean free path based on this model is too short in Cu at low energy; part of the difficulty may be due to the overestimate of the free-electron charge densities. The correlated Debye model works well for SS paths, but may give substantial errors for MS paths.

Presently, there are two parameters remaining in the theory, assuming the DW factors are known approximately, e.g., from thermal measurements. The uncertainty in the Fermi energy which determines the threshold wave vector $k = 0$ is found to be within a few eV; the value of the threshold energy E_0 is usually within a few tens of eV on an absolute energy scale. The other parameter is the amplitude reduction factor S_0^2, which is uncer-

tain to about ± 20%; attempts to calculate this quantity are in progress. We regard the MS DW factors, the self-energy near threshold, the calculation of the atomic background absorption μ_0, and the magnitude and energy dependence of the many-body amplitude factor S_0^2, as the biggest remaining uncertainties.

ACKNOWLEDGMENTS

We thank M. Newville, E. Stern, A. Hitchcock, and T. Tyliszczak for making available their experimental data. We gratefully acknowledge comments and suggestions from K. Baberschke, M. Benfatto, C. Booth, F. Bridges, G. Brown, C. Bouldin, D. Chandesris, G. George, E. Hudson, M. Newville, C. R. Natoli, P. O'Day, G. Pfeiffer, B. Ravel, D. Sayers, E. Stern, H. Wende, J. Wong, Y. Yacoby, and many users of the FEFF codes. This work was supported in part by DOE Grant No. DE-FG06-ER45415; DOE also provided some computer time.

APPENDIX A: PATH ENUMERATION AND FILTERING

The path enumeration and filtering algorithm introduced here constructs MS paths with total path length less than $2R_{\mathrm{max}}$ in an arbitrary (aperiodic) cluster. The paths so constructed are examined at various points in the process and only those necessary for convergence are kept. We begin with a list of atomic coordinates of all N_{at} atoms in a cluster and a specified central atom. A scattering path is defined by a sequence of indices $(0ijk0)$, where this notation means that the scattering path begins at the absorbing atom 0, and the photoelectron scatters successively from atoms labeled i, j, and k, before returning to the central atom 0. We define $r(jk0)$ to be the distance along the path from atom j to atom k and then to the absorbing atom 0. Given some path $(0\cdots jk0)$, we will want to make two modifications. The first is to make the shortest possible extension path of the form $(0\cdots jkl0)$, obtained by adding a new atom l to the end of the existing path. The second is to make a new path of the form $(0\cdots jk'0)$ with $r(0ijk0) \leq r(0ijk'0)$ by replacing the last scattering atom. When constructing a path of this second type, the last scattering atom will be chosen so that the entire path is at least as long as the original path and it is the atom that causes the least increase in the total path. Observe that these two path operators, extension and alteration, always yield paths that are at least as long as the given path. Using a neighbor table of $r(jk0)$ sorted by distance for all atoms j, k in the problem, we can always make these two modifications. This table requires N sorts of N items. We use a heap sort. A heap is a partially ordered data structure with the property that the smallest element in the collection can be accessed instantly and adding or removing an item to a collection of size M takes $O(\log_2 M)$ operations.[45,46] Thus, the sort requires $O(N \log_2 N)$ steps, and hence the construction of the table takes $O(N^2 \log_2 N)$ steps. For typical problems with at most a few hundred atoms, this sort algorithm takes only a few CPU seconds on a Sun SPARC Station.

Starting with the shortest path in the problem (SS from the nearest neighbor), we extend the path in the two ways described above and put both new paths ("children" of the original or "parent" path) into a heap. Here we follow the nomenclature of standard computer science sorting algorithms[46] applied to the path tree. For example, the terms parent and children refer to a given path and its descendents, respectively, in analogy with the entries in a family tree. We then remove the shortest path from the heap, write it to output, create its two children using the above two modifications, and again put the children into the heap. Again, the shortest path in the heap is removed, the two children created and added to the heap, and so on.

This algorithm will generate every path exactly once in order of increasing path length. Note that each path has a unique parent. Consider path $(0ijk0)$. It started as $(0ij0)$ with an atom added to the end, becoming $(0ijl0)$. Because the neighbor table described above was constructed at the beginning of the problem, the order in which the last atom is replaced is determined, and so our path $(0ijk0)$ is constructed from $(0ijl0)$, where $(jl0)$ is immediately before $(jk0)$ in the ordered neighbor table. Furthermore, every path will eventually be generated by this process, since any path $(0ij\cdots n0)$ does have a construction path, beginning with the null path (00). This demonstrates that every possible path will be constructed exactly once. Finally, because no child is shorter than its parent path, and because paths are removed from the heap in order of increasing path length, the paths are enunerated in order of increasing path length. Note that when the length of the path at the top of the heap is R, all paths with path length $< R$ will have been constructed, but that additional paths of length exactly R may not yet have been found.

Paths of the form $(0i0j0)$ are a complication that can be handled by adding the absorbing atom to the list of scattering atoms and to the neighbor table. In the process of building paths, paths of the form $(0i00)$ will be made and added to the heap, but will pop off the heap as soon as they are formed, since they add zero length to the current path. The path $(0i00)$ is not physical and must be discarded at output, but its two children $(0ij0)$ and $(0i0k0)$ include the necessary path and must be considered.

Path filtering to remove negligible paths is done at several stages. The first place to filter paths occurs during construction — if it is possible to eliminate paths here, entire branches of paths can be eliminated. Unfortunately, forward-scattering events amplify the importance of a path, so even if a path's contribution is small, it may increase as more atoms are added. If some R_{max} is chosen, any paths with $R > R_{\mathrm{max}}$ can be safely eliminated at this point. This also avoids the potential difficulty caused by adding two paths to the heap for every path we keep, increasing memory use linearly with the number of paths. With this R_{max} filter in place, the heap is always empty at the end of the process. To implement the heap filter, C_{heap}, consider a path with n legs. Since the

first $N-2$ scatterers and legs do not change as the path is modified, this filter must pass all paths with three or fewer legs, and only the scatterers, leg lengths, and scattering angles that will not change can be used. The PWA amplitude for path Γ is

$$\chi^{\Gamma}_{\rm heap} = \frac{1}{\rho_{n-2}} \prod_{i=1}^{n-3} \frac{f(\beta_i)}{\rho_i}, \tag{A1}$$

with n, f, ρ, etc., defined as in Eq. (7), and the filter $C_{\rm heap}$ is obtained by averaging this quantity over four energy points and then normalizing to that for the first SS shell, $C_{\rm heap} = \bar{\chi}^{\Gamma}_{\rm heap}/\bar{\chi}^{(1)}_{\rm heap}$.

If, due to symmetry, two paths have the same scattering angles and the same type of scattering atoms, the contributions to the XAFS from these paths must be the same. Such paths are called degenerate. A second situation in which the contribution from two paths will be the same is path reversal (analogous to time-reversal symmetry), that is, the contributions from paths $(0ijk0)$ and $(0kji0)$ to the XAFS will be the same. The savings from removing time-reversal degeneracies is a factor of 2, and that from removing other degeneracies can be much larger.

The second place to filter paths is as paths are removed from the heap, before degeneracies are eliminated. Since degeneracies can be as large as 196 in fcc materials, this filter $C_{\rm keep}$, must be used conservatively. The mean amplitude is

$$\bar{\chi}^{\Gamma}_{\rm keep} = \frac{1}{\Delta k} \int_0^{k_{\rm max}} \frac{\rho_n}{\cos(\beta_0)} \prod_{i=1}^{n-1} \frac{f(\beta_i)}{\rho_i} dk, \tag{A2}$$

where the integral is estimated by a sum over a few energy points and $C_{\rm keep}$ is defined by normalizing this factor relative to that for the first SS path, $C_{\rm keep} = \bar{\chi}^{\Gamma}_{\rm pw}/\bar{\chi}^{(1)}_{\rm pw}$.

Degeneracy elimination is a sorting problem; since the path enumeration algorithm returns paths already sorted by path length, we check degeneracies for each set of paths with the same total path length by forming for each path a unique eight-byte number termed a "hash key"[46] and using a heap sort[45,46] on these hash keys. Thus, if two paths are degenerate, they will have the same hash key. This allows us to count degeneracies at a rate proportional to $N \log_2 N$, where N is the number of paths with a particular total path length. Cluster symmetries can also reduce the number of paths found during path enumeration. Our code optionally allows the user to specify symmetries by designating some atoms as not-allowed for the first atom in a path, and defining a degeneracy factor for the remaining atoms that are allowed to be first atoms in a path. For fcc and bcc materials, this simple algorithm can lead to time savings in the path enumeration step of order the coordination number of each shell, thus permitting calculations to very large distances. The path amplitude is invariant under all of the following symmetry operations. (1) Polarization average case: rotations about any axis and reflections in any plane containing central atom (O_3 group); (2) linear polarization: rotations only around axis parallel to $\hat{\epsilon}$ and reflections in planes containing $\hat{\epsilon}$ or normal to it ($D_{\infty h}$ group); (3) elliptical polarization: reflections in three mutually orthogonal planes normal to direction of propagation and ellipse axes (D_{2h} group). The degeneracy checker in FEFF compares two paths in terms of their coordinates in their own "standard" frame. The standard frame for each path is defined as follows. (1) Polarization average case: z axis in the direction of the first leg; the x axis is chosen in order to have $x > 0$ and $y = 0$ for the first atom not on z axis; the y axis is chosen to have a positive y coordinate for the first atom not in the xz plane; (2) linear polarization: the z axis is parallel to $\hat{\epsilon}$ and the first nonzero z coordinate is positive. The choice of x and y axes is the same; (3) elliptical polarization: the z axis is along the direction of light propagation and the x and y axes parallel to the axes of the ellipse. The positive direction of each axis is determined as above; the first nonzero component should be positive. Now we can compare paths, comparing the hash keys for "standard frame" coordinates. Between two "time-reversed" paths, we choose the one with the smaller hash key. We also check for possible hash collisions. After removing the degeneracies, much more accurate filters can be used. The fast plane-wave filter $C_{\rm pw}$ is the same as $C_{\rm keep}$ except that degeneracies are included. The PWA simply replaces the RA scattering matrices with 1×1 matrices and uses a look up table of scattering angles and amplitudes for each atomic species. Hence, a few floating point operations are sufficient to approximate the XAFS to within about 30% or so. For typical problems, setting this filter $C_{\rm pw}$ to 2.5% is sufficient to reduce the number of paths to perhaps a few hundred, without eliminating any important ones. Finally, the last filtering step takes place after the full curved-wave XAFS calculation has been done. The mean curved-wave amplitude is

$$\bar{\chi}^{\Gamma}_{\rm cw} = \frac{1}{\Delta k} \int_0^{k_{\rm max}} |\chi^{\Gamma}(k)| dk, \tag{A3}$$

where the integral is approximated over nine evenly spaced k points, and $\chi^{\Gamma}(k)$ is the full curved-wave calculation for path Γ, including degeneracy, mean free path, etc. The curved-wave filter $C_{\rm cw} = \bar{\chi}^{\Gamma}_{\rm cw}/\bar{\chi}^{(1)}_{\rm cw}$ is normalized by the value at the first-neighbor distance and expressed as a %. This filter does not save any computation time in path enumeration, but by eliminating the remaining unimportant paths, it greatly simplifies the analysis, and it provides a quick estimate of actual path importance.

APPENDIX B: POLARIZATION DEPENDENCE

In this appendix we discuss how general elliptical polarization dependence in XAFS within the dipole approximation can be calculated for all shells with the RA curved-wave scattering-matrix formalism.[21] From RA, we have

$$\chi_l(\hat{\epsilon}, k) = {\rm Im} \sum_{L_n, L_0} G_{L_n, L_0}\, e^{i\delta_{l_n} + i\delta_{l_0}} \times \frac{\sum_m \langle L\mathbf{0}|\hat{\epsilon}^* \cdot \mathbf{r}|L_n\mathbf{0}\rangle \langle L_0\mathbf{0}|\hat{\epsilon} \cdot \mathbf{r}|L\mathbf{0}\rangle}{\sum_{m,L'} \langle L\mathbf{0}|\hat{\epsilon}^* \cdot \mathbf{r}|L'\mathbf{0}\rangle \langle L'\mathbf{0}|\hat{\epsilon} \cdot \mathbf{r}|L\mathbf{0}\rangle}, \tag{B1}$$

where L_n and L_0 are the final and initial angular momenta of the electron, $L = (l, m)$, $\hat{\epsilon}$ is the polarization vector, which is generally complex to allow for general elliptic polarization; i.e., $\hat{\epsilon} = \epsilon' + i\epsilon''$ where the ratio $|\epsilon''|/|\epsilon'|$ is the ellipticity and $\epsilon' \times \epsilon''$ is along the propagation direction $\hat{k}$ of the x-ray beam, $G_{L_n,L_0} = \langle L_n|G|L_0\rangle$ is the matrix element of the total dimensionless propagator, which is equal to the sum over contributions from all different MS paths $G_{L_n,L_0} = \sum_\Gamma G^{(n-1)}_{L_n,L_0}(\mathbf{R}_1, \ldots, \mathbf{R}_n)$. The expression for $G_{L_n,L_0}(\Gamma) = G^{(n-1)}_{L_n,L_0}(\mathbf{R}_1, \ldots, \mathbf{R}_n)$ is given by Eq. (15) in RA, i.e., $G_{L_n,L_0}(\Gamma) = [e^{i(\rho_1+\rho_2+\cdots\rho_n)}/\rho_1\rho_2\cdots\rho_n]\mathrm{Tr}_\lambda \quad M^{L_0,L_n}F^{n-1}\ldots F^2F^1$ The sum in the denominator can be done using properties of the 3j symbols, giving a factor 3 in the following formulas,

$$\chi(\hat{\epsilon},k) = \mathrm{Im}\sum_{m's} G_{L_n,L_0}\, e^{2i\delta_{l_0}}\, S_{l_n,l_0}(k) \times \sum_{\alpha,\beta=-1}^{1} 3(\epsilon_\alpha)^*\epsilon_\beta \begin{pmatrix} l & 1 & l_n \\ -m & \alpha & m_n \end{pmatrix} \times \begin{pmatrix} l & 1 & l_0 \\ -m & \beta & m_0 \end{pmatrix}, \tag{B2}$$

where $S_{l_n,l_0}(k) = \langle l\|r\|l_n\rangle\,\langle l\|r\|l_0\rangle/(\langle l\|r\|l-1\rangle^2 + \langle l\|r\|l+1\rangle^2)$ is a function of reduced matrix elements, which depends on the photoelectron energy. By definition, $S_{l+1,l+1}(k) + S_{l-1,l-1}(k) = 1$. Here, for simplicity, we illustrate the method with a nonrelativistic treatment (the relativistic treatment in terms of spinors used in FEFF is analogous) so

$$\langle l\|r\|l'\rangle = (-)^l\left[\frac{3\,(2l+1)(2l'+1)}{4\pi}\right]^{1/2} \times \begin{pmatrix} l & 1 & l' \\ 0 & 0 & 0 \end{pmatrix} \int dr\, r^3\, y_l(r)\, y_{l'}(r), \tag{B3}$$

where $y_l(r)$ is regular normalized solution of the Schrödinger equation. Note that $\langle l\|r\|l_n\rangle = -\langle l_n\|r\|l\rangle$. We can express S_{l_n,l_0} through the ratio of reduced matrix elements $f = \langle l\|r\|l-1\rangle/\langle l\|r\|l+1\rangle$ as $S_{l_n,l_0} = f^{(l+1-l_n+l+1-l_0)/2}/(1+f^2)$. The factor $S_{l_n,l_0} = 0$ if either l_n or l_0 not equal to $l \pm 1$. In the case of linear polarization, $\hat{\epsilon}$ is a real vector ($\hat{\epsilon}^* = \hat{\epsilon}$) and Eq. (B2) can be rewritten as

$$\chi(\hat{\epsilon},k) = \mathrm{Im}\sum_{\mu,L_n,L_0} G_{L_n,L_0}\, e^{i\delta_{l_n}+i\delta_{l_0}}\, S_{l_n,l_0} \times \sum_{\mu=-l}^{l} 3\begin{pmatrix} l & 1 & l_n \\ \mu & 0 & \mu \end{pmatrix}\begin{pmatrix} l & 1 & l_0 \\ \mu & 0 & \mu \end{pmatrix} \times R^{l_0}_{m_0,\mu}(\Omega_{\hat{\epsilon}^{-1}})\; R^{l_n}_{\mu,m_n}(\Omega_{\hat{\epsilon}}), \tag{B4}$$

where we have used the relation $\langle L|\hat{\epsilon}\cdot\mathbf{r}|L'\rangle = \sum_{\mu=-l}^{1} \mathrm{R}^1_{\mathrm{m},\mu}(\Omega_{\hat{\epsilon}^{-1}})\langle l,\mu|z|l',\mu\rangle \mathrm{R}^{l'}_{\mu,\mathrm{m}'}(\Omega_{\hat{\epsilon}})$ and performed the sum over m. The argument $\Omega_{\hat{\epsilon}}$ represents the Euler rotation of the polarization vector $\hat{\epsilon}$ onto the z axis, namely, $(\alpha\beta\gamma) = (0,\theta,\pi-\phi)$, where θ and ϕ are the polar angles of the vector $\hat{\epsilon}$ (See footnote 1, p. 1073 of Messiah[66]). From Eq. (15) of RA, Eq. (B2) can be rewritten using the matrices $F_{\lambda\lambda'}(\rho,\rho')$ and a "termination matrix" $M^{L_0,L_n}_{\lambda\lambda'}(\rho_1,\rho_n)$ defined by Eq. (16) and (17) in RA, which depends only on properties at the absorption site,

$$M_{\lambda\lambda'}(\hat{\epsilon},\rho_1,\rho_n) = \sum_{\alpha,\beta,m,L_n,L_0} 3\,(\epsilon_\alpha)^*\epsilon_\beta \times \begin{pmatrix} l & 1 & l_n \\ -m & i & m_n \end{pmatrix}\begin{pmatrix} l & 1 & l_0 \\ -m & j & m_0 \end{pmatrix} \times S_{l_n,l_0}\, M^{L_0,L_n}_{\lambda\lambda'}(\rho_1,\rho_n) = \sum_{\alpha,\beta}(\epsilon_\alpha)^*\epsilon_\beta M_{\alpha,\beta}. \tag{B5}$$

From Eqs. (B4) and (B5) we obtain $\chi(\hat{\epsilon}) = \sum_{\alpha,\beta}(\epsilon_\alpha)^*\epsilon_\beta\chi_{\alpha,\beta}(k)$, which is the form given in Eq. (5). Thus, only small adjustments to the existing code FEFF5 were needed to handle the polarized case. This included adding an extra "fictitious leg" $\hat{\epsilon}$ at the central atom and a subroutine to make the "polarization tensor" $[(\epsilon_\alpha)^*\epsilon_\beta + \epsilon_\alpha(\epsilon_\beta)^*]/2$. The average of left and right elliptical polarizations is taken in order to have identical contributions from "time-reversed" paths. This procedure is exact because the absorption coefficient must be the same for left and right elliptical polarizations in the absence of magnetism. The expression in Eq. (B5) was used to modify the existing polarization average code FEFF5. The transition $(l \to l-1)$ is neglected in the present version of code which is exact for $l = 0$ shells and an acceptable approximation for L shells. Finally, we note that these formulas are only valid for nonmagnetic materials for which the effective Hamiltonian is spin independent. The case for x-ray circular magnetic dichroism will be discussed separately.[67]

[1] P. A. Lee and J. B. Pendry, Phys. Rev. B **11**, 2795 (1975).

[2] *X-Ray Absorption: Principles, Applications, Techniques of EXAFS, SEXAFS, and XANES*, edited by D. C. Koningsberger and R. Prins (Wiley, New York, 1988).

[3] J. J. Rehr, C. H. Booth, F. Bridges, and S. I. Zabinsky, Phys. Rev. B **49**, 12 347 (1994).

[4] B. W. Holland, J. B. Pendry, R. F. Pettifer, and J. Bordas, J. Phys. C **11**, 633 (1978).

[5] J. J. Rehr, R. C. Albers, and S. I. Zabinsky, Phys. Rev. Lett. **69**, 3397 (1992).

[6] S. Doniach, M. Berding, T. Smith, and K. O. Hodgson, in *EXAFS and Near Edge Structure III*, edited by K. O. Hodgson, B. Hedman, and J. E. Penner-Hahn (Springer-Verlag, Berlin, 1984), p. 33.

[7] T. A. Tyson, K. O. Hodgson, C. R. Natoli, and M. Benfatto, Phys. Rev. B **46**, 5997 (1992).

[8] J. J. Rehr, Jpn. J. Appl. Phys. **32**, 8 (1993).

[9] P. J. Durham, J. B. Pendry, and C. H. Hodges, Comput.

Phys. Commun. **25**, 193 (1982).
[10] D. D. Vvendensky, D. K. Saldin, and J. B. Pendry, Comput. Phys. Commun. **40**, 421 (1986).
[11] G. Bunker and E. A. Stern, Phys. Rev. Lett. **52**, 1990 (1984).
[12] S. J. Gurman, N. Binsted, and I. Ross, J. Phys. C **19**, 1845 (1986).
[13] R. V. Vedrinskii and L. A. Bugaev, J. Phys. B **24**, 1967 (1991).
[14] R. C. Albers, A. K. McMahan, and J. E. Müller, Phys. Rev. B **31**, 3435 (1985).
[15] J. E. Muller, O. Jepsen, O. K. Andersen, and J. W. Wilkins, Phys. Rev. Lett. **40**, 720 (1978).
[16] J. E. Muller, O. Jepsen, and J. W. Wilkins, Solid State Commun. **42**, 365 (1982).
[17] J. E. Muller and J. W. Wilkins, Phys. Rev. B **29**, 4331 (1984).
[18] D. E. Ellis and G. L. Goodman, Int. J. Quantum Chem. **XXV**, 185 (1984).
[19] A. D. Cicco and A. Filipponi, Phys. Rev. B **49**, 12 564 (1988).
[20] T. Fujikawa, J. Phys. Soc. Jpn. **62**, 2155 (1993).
[21] J. J. Rehr and R. C. Albers, Phys. Rev. B **41**, 8139 (1990).
[22] J. Mustre de Leon, Ph.D. thesis, University of Washington, 1989.
[23] J. J. Rehr, J. Mustre de Leon, S. I. Zabinsky, and R. C. Albers, J. Am. Chem. Soc. **113**, 5135 (1991).
[24] J. Mustre de Leon, J. J. Rehr, S. I. Zabinsky, and R. C. Albers, Phys. Rev. B **44**, 4146 (1991).
[25] S. I. Zabinsky, J. Mustre de Leon, J. J. Rehr, and R. C. Albers (unpublished); those interested in obtaining the FEFF codes should contact the authors.
[26] M. Newville, B. Ravel, D. Haskel, E. A. Stern, and Y. Yacoby, Physica B **208&209**, 154 (1995).
[27] G. J. George (unpublished).
[28] C. Dagg, L. Tröger, C. Arvantis, and K. Baberschke, J. Phys. Condens. Matter **5**, 6845 (1993).
[29] P. A. O'Day, J. J. Rehr, S. I. Zabinsky, and G. E. Brown, Jr., J. Am. Chem. Soc. **116**, 2938 (1994).
[30] O. Heckmann, H. Magnan, P. le Fevre, D. Chandesris, and J. J. Rehr, Surf. Sci. **312**, 62 (1994).
[31] A. I. Frenkel, E. A. Stern, M. Qian, and M. Newville, Phys. Rev. B **48**, 12 449 (1993).
[32] G. Pfeiffer, J. J. Rehr, and D. E. Sayers, Phys. Rev. B **51**, 804 (1995).
[33] M. Newville, P. Līviņš, Y. Yacoby, J. J. Rehr, and E. A. Stern, Phys. Rev. B **47**, 14 126 (1993).
[34] H. Stragier, J. O. Cross, J. J. Rehr, L. B. Sorensen, C. E. Bouldin, and J. C. Woicik, Phys. Rev. Lett. **69**, 3064 (1992).
[35] A. P. Kaduwela, D. J. Friedman, and C. S. Fadley, J. Electron Spectrosc. Relat. Phenom. **57**, 223 (1991).
[36] S. I. Zabinsky, Ph.D. thesis, University of Washington, 1993.
[37] U. von Barth and G. Grossmann, Phys. Rev. B **25**, 5150 (1982).
[38] T. L. Loucks, *Augmented Plane Wave Method* (Benjamin, New York, 1967).
[39] D. D. Koelling and B. N. Harmon, J. Phys. C **10**, 3107 (1977); also, see, H. L. Skriver, *The LMTO Method* (Springer-Verlag, Berlin, 1984), Chap. 9.6.1, pp. 219–221.
[40] V. Fritzsche, J. Electron Spectrosc. Relat. Phenom. **58**, 299 (1992).
[41] N. Binsted and D. Norman, Phys. Rev. B **49**, 15 531 (1994).
[42] E. A. Stern, D. E. Sayers, and F. W. Lytle, Phys. Rev. B **11**, 4836 (1975).
[43] O. Keski-Rahkonen and M. O. Krause, At. Data Nucl. Data Tables **14**, 140 (1974).
[44] R. G. Newton, *Scattering Theory of Waves and Particles*, 2nd ed. (Springer, New York, 1982).
[45] D. E. Knuth, *The Art of Computer Programming* (Addison-Wesley, New York, 1973), Vol. 3.
[46] R. Sedgewick, *Algorithms in C++* (Addison-Wesley, New York, 1992).
[47] J. P. Desclaux, Comput. Phys. Commun. **9**, 31 (1975).
[48] L. F. Mattheiss, Phys. Rev. **133**, A1399 (1964).
[49] J. J. Quinn, Phys. Rev. **126**, 1453 (1962).
[50] E. Sevillano, H. Meuth, and J. J. Rehr, Phys. Rev. B **20**, 4908 (1979).
[51] P. Rennert, J. Phys. C **4**, 4315 (1992).
[52] E. D. Crozier, J. J. Rehr, and R. Ingalls, in *X-Ray Absorption: Principles, Applications, Techniques of EXAFS, SEXAFS, and XANES* (Ref. 2), pp. 375–384.
[53] A. I. Frenkel and J. J. Rehr, Phys. Rev. B **48**, 585 (1993).
[54] G. Beni and P. M. Platzman, Phys. Rev. B **14**, 9514 (1976).
[55] J. Stöhr, *NEXAFS Spectroscopy* (Springer, Heidelberg, 1992).
[56] C. R. Natoli, in *EXAFS and Near Edge Structure*, edited by A. Bianconi (Springer, New York, 1983), p. 43.
[57] M. Newville, Ph.D. thesis, University of Washington, 1994.
[58] M. Benfatto, C. R. Natoli, and A. Filipponi, Phys. Rev. B **40**, 9636 (1989).
[59] D. R. Penn, Phys. Rev. B **35**, 482 (1987).
[60] A. P. Hitchcock, J. D. Garrett, and T. Tyliszczak, J. Phys. (Paris) Colloq. **47**, C8-1081 (1986).
[61] T. Tyliszczak, P. Aebi, and A. P. Hitchcock (unpublished); the thin single crystal is courtesy of E. Dartyge and A. Sadoc (LURE).
[62] J. J. Rehr, Surf. Rev. Lett. **2**, 63 (1995).
[63] H. Wende, J. J. Rehr, D. Arvanitis, L. Tröger, T. Lederer, M. Tischer, K. Baberschke, A. Ankudinov, M. Newville, and S. I. Zabinsky (unpublished).
[64] E. A. Stern, B. A. Bunker, and S. M. Heald, Phys. Rev. B **21**, 5521 (1980).
[65] A. Filipponi and S. Mobilio, Phys. Rev. B **38**, 3298 (1988).
[66] A. Messiah, *Quantum Mechanics* (Wiley, New York, 1966).
[67] A. Ankudinov and J. J. Rehr (unpublished).